A&A 597, A45 (2017)
DOI: 10.1051/0004-6361/201629289

Astronomy & Astrophysics

Deuterium fractionation of a distant cold dark cloud along the line of sight of W51★

C. Vastel[1,2], B. Mookerjea[3], J. Pety[4], and M. Gerin[5,6]

[1] Université de Toulouse, UPS-OMP, IRAP, 31400 Toulouse, France
e-mail: charlotte.vastel@irap.omp.eu
[2] CNRS, IRAP, 9 Av. Colonel Roche, BP 44346, 31028 Toulouse Cedex 4, France
[3] Tata Institute of Fundamental Research, Homi Bhabha Road, 400005 Mumbai, India
[4] Institut de Radioastronomie Millimétrique, 300 rue de la Piscine, 38406 Saint-Martin d'Hères, France
[5] LERMA, Observatoire de Paris, PSL Research University, CNRS, UMR 8112, 75014 Paris, France
[6] Sorbonne Universités, UPMC Univ. Paris 06, UMR 8112, LERMA, 75005 Paris, France

Received 11 July 2016 / Accepted 14 November 2016

ABSTRACT

Herschel/HIFI observations toward the compact HII region W51 has revealed the presence of a cold dense core along its line of sight in a high-velocity stream located just in front of W51. This detection has been made possible through absorption measurements of low-energy transitions of HDO, NH_3, and C_3 against the bright background emitted by the star-forming region. We present a follow-up study of this core using the high sensitivity and high spectral resolution provided by the IRAM 30m telescope. We report new detections of this core in absorption for DCO^+ (2–1, 3–2), $H^{13}CO^+$ (1–0), DNC (3–2), $HN^{13}C$ (1–0), p-H_2CO ($2_{0,2}$–$1_{0,1}$, $3_{0,3}$–$2_{0,2}$), and in emission for o-NH_2D. We also report interferometric observation of this last species using the IRAM/NOEMA telescope, revealing the fragmented nature of the source through the detection of two cores, separated by 0.19–0.24 pc, with average sizes of less than 0.16–0.19 pc. From a non-LTE analysis, we are able to estimate the density (~2.5×10^4 cm^{-3}) and temperature (~10 K) of this component, typical of what is found in dark clouds. This component (called W51-core) has the same DCO^+/HCO^+ ratio (0.02) as TMC-1 and a high DNC/HNC ratio (0.14). Detection of these deuterated species indicates that W51-core is similar to an early-phase low-mass star-forming region, formed from the interaction between the W51 giant molecular cloud and the high-velocity stream in front of it. The W51 complex being at about 5 kpc, these findings lead to what is the first detection of the earliest phase of low-mass star-forming region at such a large distance.

Key words. astrochemistry – line: identification – molecular data – radiative transfer

1. Introduction

The unprecedented sensitivity and large-scale mapping capabilities of *Herschel*/SPIRE have revealed a large network of parsec-scale filaments in Galactic molecular clouds, which indicate an intimate connection between the filamentary structure of the interstellar medium (ISM) and the formation of dense cloud cores (André et al. 2010; Molinari et al. 2010). Since star formation occurs mostly in prominent filaments, characterizing the physical properties of these regions is the key to understanding the process of star formation.

We have recently detected a dense core for the first time along the line of sight of the compact HII region W51 (Mookerjea et al. 2014). Having no information on the spatial extent of this core, we could not distinguish between a core (0.03–0.2 pc) or a clump (0.3–3 pc). Located at a distance of $5.41^{+0.31}_{-0.28}$ kpc (Sato et al. 2010), W51 is a radio source with a complicated morphology (see Sollins et al. 2004 for a sketch of the spatial distribution of the various components described below) in which many compact sources are superimposed on extended diffuse emission (Bieging 1975). The line of sight to W51 intersects the Sagittarius spiral arm nearly tangentially ($l = 49°$), which means that sources over a ~5 kpc range of distances are superimposed along the line of sight. Carpenter & Sanders (1998) divided the molecular gas associated with the W51 HII region into two subgroups: a giant molecular cloud (1.2×10^6 $M_\odot$) at V_{LSR} ~ 61 km s^{-1}, and an elongated (22×136 pc) molecular cloud similar to a filamentary structure (1.9×10^5 $M_\odot$) at 68 km s^{-1}. Koo (1997) used HI observations toward W51e2 to identify two sets of absorption features, the local features at 6.2, 11.8, and 23.1 km s^{-1} and features thought to belong to the Sagittarius spiral arm at 51.1, 62.3, and 68.8 km s^{-1}. The massive star formation activity in the W51 region is believed to have resulted from a collision between the W51 giant molecular cloud and the high-velocity (HV; 68 km s^{-1}) cloud (Carpenter & Sanders 1998; Kang et al. 2010). Using H_2CO observations, Arnal & Goss (1985) detected five absorption components at ~52, 55, 57, 66, and 70 km s^{-1} toward W51e2. The presence of H_2CO absorption between 66 and 70 km s^{-1} and of H I absorption at 68.8 km s^{-1} implies that the HV stream is located in front of W51e.

The dense core was detected as an absorption feature at ~69 km s^{-1} toward the compact HII region W51e2 in transitions of HDO, CN, NH_3, CCH, c-C_3H_2, and C_3 (Mookerjea et al. 2014). This was the first ever detection of HDO in an environment outside low- and high-mass star-forming regions. Among the species detected in the dense core, HDO, o- and p-NH_3, and

★ IRAM 30m data are only available at the CDS via anonymous ftp to cdsarc.u-strasbg.fr (130.79.128.5) or via http://cdsarc.u-strasbg.fr/viz-bin/qcat?J/A+A/597/A45

C_3 show line widths between 1.5–2 km s^{-1}, while the lines of CN and CCH are narrower (0.6–0.7 km s^{-1}). Non-local thermodynamic equilibrium (LTE) RADEX modeling of CN and NH_3 also indicate the presence of two components contributing to the absorption: NH_3 arises from the denser (5×10^5 cm^{-3}) and warmer (30 K) gas, while CN arises from a less dense (10^5 cm^{-3}) and cooler medium (6–10 K). We thus concluded that the 69 km s^{-1} feature arises in a dense and cold core that is formed within the much larger scale filament, deemed to be interacting with the W51 main molecular cloud. A possible scenario for formation of the dense core was suggested based on the collision of the filament with W51 (Kang et al. 2010). In this scenario, cloud-cloud collisions lead to the compression of the interface region and initiate the formation of stars, causing the molecular cores at the interface to be heated, but leaving the cores on the trailing side cold (Habe & Ohta 1992).

Based on the available observations, Mookerjea et al. (2014) ascertained the abundances of all detected species in the 69 km s^{-1} absorption feature. The abundances are similar to those found in the prestellar and protostellar cores. The D/H ratio for water vapor is 9.6×10^{-4}, similar to the value found in Orion KL (Neill et al. 2013) and also similar to the value found in the cold envelope of the IRAS 16293-2422 low-mass star-forming region (Coutens et al. 2012, 2013) where the ices are not affected by thermal desorption or photo-desorption by the FUV field.

In this paper we present observations from the IRAM NOEMA and 30m telescopes of several tracers (focused on deuterium chemistry) toward the newly detected cold dense core to uncover the conditions prevailing in this filament and also to probe the degree of deuteration in the core.

2. Observations

2.1. IRAM 30m observations

The observations were performed at the IRAM 30m telescope toward W51 (α_{2000} = 19^{h}23^{m}43.9^s, δ_{2000} = 14°30′30.5″) between July 16, 2013, and July 19, 2013. We used the broadband receiver EMIR connected to an FTS spectrometer in its 50 kHz resolution mode. The beam of the observations is 29″, 23″, and 11″ at 86, 106, and 210 GHz, respectively. Weather conditions were average with 2 to 3 mm of precipitable water vapor. In order to obtain a flat baseline, observations were carried out using a nutating secondary mirror with a throw of 3 arcmin. No contamination from the reference position was observed.

Pointing was checked every 1.5 h on the nearby continuum sources 1923+210, 1749+096, and 1757−240. We adopted the telescope and receiver parameters (main-beam efficiency, half power beam width, forward efficiency) from the values monitored at IRAM[1].

Figure 1 presents the IRAM 30m observations of all the species unambiguously detected in our observations along with the *Herschel*/HIFI HDO detection from Mookerjea et al. (2014). A red dashed line indicates the location of the core at 69.5 km s^{-1}. Line intensities are expressed in units of antenna temperatures, before correction for the main beam efficiencies. The continuum has been subtracted and its values are quoted in Table 1. Table 1 lists the spectroscopic parameters of the detected transitions, the spectral resolution (ΔV), as well as the properties of the observed transitions based on Gaussian fitting of the lines: $V_{\rm center}$ (velocity centroid of the Gaussian fitting function),

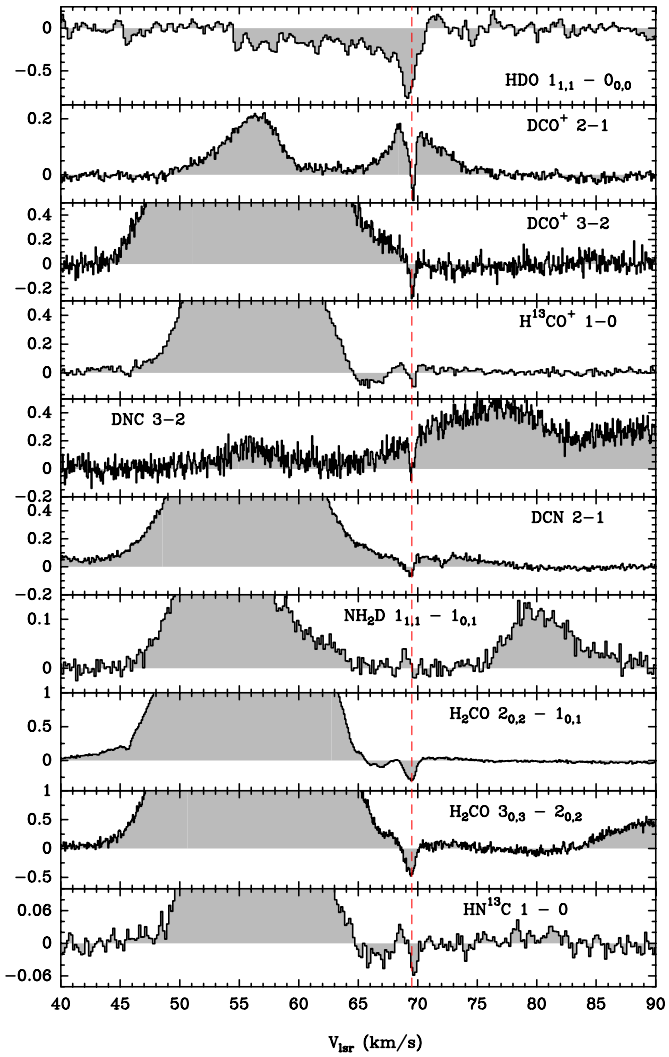

Fig. 1. *Herschel*/HIFI (HDO) and IRAM 30m observations (in T_A^*). The red vertical dashed line indicates the location of the core at a velocity of 69.5 km s^{-1}.

T_C (continuum value), FWHM (full width at half maximum). The integrated opacity for the absorption lines is calculated in Col. 9 and is computed as

$$\int \tau_{\rm obs} dV = -\int \ln \frac{T_{\rm mb}}{T_C} dV. \quad (1)$$

If the line is in emission, Col. 9 simply states the integrated area in K km s^{-1}, assuming that the foreground core responsible for the absorption of the continuum is more extended than the continuum emitting region. Indeed, as long as the size of the absorbing layer is larger than the size of the region emitting the continuum, the line-to-continuum ratio does not depend on the sizes of the telescope beam used for the observations. We used the CASSIS[2] software (Vastel et al. 2015), developed at IRAP, for the line identification.

2.2. IRAM NOEMA observations

To resolve the spatial distribution of the source that shows narrow absorption of deuterated species, we obtained additional

[1] http://www.iram.fr

[2] http://cassis.irap.omp.eu

Table 1. Properties of the observed transitions at the IRAM 30m telescope.

Species	Transitions	Frequency (MHz)	ΔV (km s^{-1})	E_{low} (K)	E_{up} (K)	V_{center} (km s^{-1})	T_C K	$FWHM$ (km s^{-1})	$\int \tau_{obs} dV$ or area (km s^{-1}) or (K km s^{-1})	rms (mK)
DCO^+	2–1	144 077.2890	0.10	3.46	10.37	69.58 ± 0.02	1.08	0.40 ± 0.05	0.17 ± 0.03	14.8
DCO^+	3–2	216 112.5822	0.07	10.37	20.74	69.56 ± 0.03	2.58	0.36 ± 0.06	0.12 ± 0.02	89.8
$H^{13}CO^+$	1–0	86 754.2884	0.17	0.00	4.16	69.64 ± 0.10	0.93	0.34 ± 0.11	0.11 ± 0.02	20.0
DNC	3–2	228 910.4810	0.07	11.00	21.97	69.52 ± 0.03	2.54	0.42 ± 0.06	0.09 ± 0.01	99.9
$HN^{13}C$	1–0	87 090.8252	0.17	0.00	4.18	69.70 ± 0.03	0.93	0.54 ± 0.07	0.010 ± 0.002	16.2
o-NH_2D	$1_{1,1}$–$1_{0,1}$	85 926.2780	0.17	16.56	20.68	68.91 ± 0.06	1.20	0.58 ± 0.15	0.020 ± 0.003[a]	15.7
p-H_2CO	$2_{0,2}$–$1_{0,1}$	145 602.9490	0.10	3.50	10.48	69.38 ± 0.02	1.08	0.93 ± 0.04	0.50 ± 0.08	24.9
p-H_2CO	$3_{0,3}$–$2_{0,2}$	218 222.1920	0.07	10.48	20.96	69.39 ± 0.03	2.42	0.78 ± 0.06	0.39 ± 0.06	78.4

Notes. The spectroscopic parameters are from CDMS. Data are available at the CDS. [(a)] Only transition detected in emission.

Table 2. Properties of the observed NH_2D transition at the IRAM Plateau de Bure interferometer.

Location	V_{center} (km s^{-1})	Area (mK km s^{-1})	$FWHM$ (km s^{-1})	T_{peak} (mK)
Ellipse A	68.90	150.2	1.20	117.58
Ellipse B	68.54	100.3	0.57	164.45
Other	68.25	13.1	0.30	40.91
	68.85	33.8	0.55	57.71

observations of the o-NH_2D emission from the NOEMA interferometer in C and D configurations. We obtained 10 h of usable on-source data (time computed for an eight-antenna array). Weather varied from excellent to average. The achieved resolution is $5.36 \times 4.77''$ at a position angle of $-20.4°$. The lower sideband of the 3 mm receivers was tuned at 85.926 GHz. One of the narrowband correlator windows was centered at the frequency of the o-NH_2D line (85.926 GHz) yielding 20 MHz-wide spectra at 39 kHz (or 0.14 km s^{-1}) channel spacing. We observed a single field centered on the M51 HII compact region. The NOEMA primary beam size is typically 59″ at the observing frequency.

MWC 349 was used as flux calibrator, 1920+154 and 1932+204 as phase/amplitude calibrators, and 3C 454.3 as bandpass calibrator. Data calibration and imaging/deconvolution used the standard procedures of the CLIC and MAPPING software of the GILDAS suite[3]. Data was self-calibrated in phase on the strong continuum source toward W51. No short-spacing corrections were applied.

As shown in Fig. 2, the NH_2D emission integrated between 68.1 and 69.0 km s^{-1} is fragmented into several peaks. Two marginally resolved sources (A and B) are clearly detected. About 15% of the total flux is scattered outside these two main sources. The NH_2D line sits between two wide lines, identified as CH_3OCHO (7(6, 2)–6(6, 1)) at 85.927 GHz and CH_3OCHO (7(6, 1)–6(6, 0)) at 85.919 GHz. Both lines are emitted at the velocity of the W51 HII region (~55 km s^{-1}).

Table 2 presents the observational properties of both fragments, integrated over two ellipses $10 \times 7''$ and $8 \times 6''$ in size for A and B, respectively. The IRAM 30m beam size is 30.2″. This gives beam dilution factors of 13 and 19, respectively. Applying these factors to the measured integrated intensities, we find that we recover 17 mK km^{-1}, i.e., the intensity measured at the resolution of the IRAM 30m, within the uncertainties.

[3] See http://www.iram.fr/IRAMFR/GILDAS/ for more details on the GILDAS software.

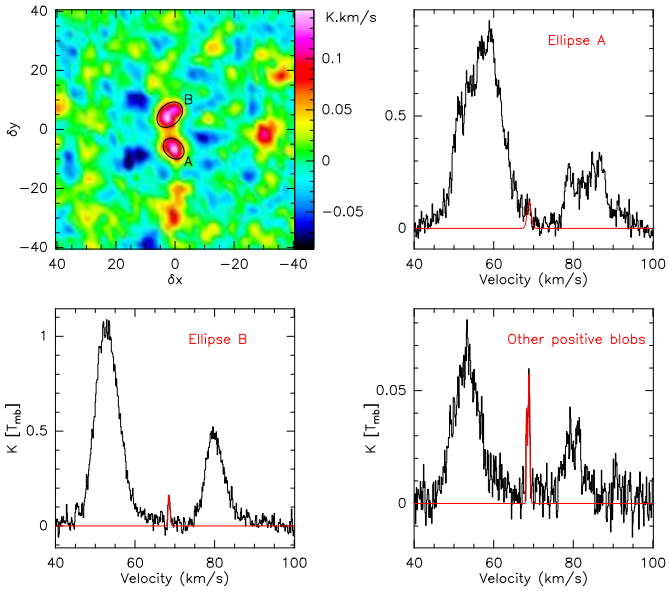

Fig. 2. Results from the NOEMA observations for the NH_2D transition at 86 GHz. *Top left*: line intensity integrated between 68.1 and 69.0 km s^{-1}. *Top right*: spectra integrated over ellipse A. *Bottom left*: spectra integrated over ellipse B. *Bottom right*: spectra integrated over all pixels of the top left image whose integrated intensity belongs to the [0.025, 0.2 K km s^{-1}] range, except pixels inside ellipse A and B.

3. Discussion

3.1. Radiative transfer modeling

From Mookerjea et al. (2014), we were able to identify two physical components: one warm component (30 K) with a H_2 density of 5×10^5 cm^{-3} detected through NH_3 measurements, while the other component is less dense (10^5 cm^{-3}) with a lower kinetic temperature (6 K), detected with CN. However, owing to the complexity of the line profiles (see Figs. 3 and 4 from Mookerjea et al. 2014), which were explained by the contamination by the molecular cloud complex between 55 and 70 km s^{-1}, the H_2 density and kinetic temperature estimated from non-LTE modeling have a large error bar (valid to within 50%).

For the following analysis we used the CASSIS software, which performs LTE and non-LTE modeling and list in Table 3 the results from our radiative transfer analysis. In the present observations, DCO^+ 2–1 seen in absorption is blended with an emission line from CH_3OCHO (21(3, 18)–21(2, 19)) at 144.070 GHz emitted at the velocity of the HII region at

Table 3. Column densities and abundances derived from LTE or non-LTE radiative transfer.

Species	V_{LSR} (km s^{-1})	T_{ex} (K)	T_k (K)	$n(H_2)$ (cm^{-3})	N (cm^{-2})
DCO^+	69.58	3.5[a]	10	2.5×10^4	5×10^{11}
$H^{13}CO^+$	69.64	3.5	10	2.5×10^4	4×10^{11}
DNC	69.52	3.0[b]	10	2.5×10^4	1.2×10^{12}
$HN^{13}C$	69.70	3.1	10	2.5×10^4	1.3×10^{11}
o-NH_2D	68.91	5–10			$0.4–1.8 \times 10^{12}$[c]
	68.90	5–10			$0.2–1.1 \times 10^{13}$[d]
	68.54	5–10			$1.3–6.9 \times 10^{12}$[e]
p-H_2CO	69.39	3.5[a]	10	2.5×10^4	5×10^{12}

Notes. [(a)] For both transitions; [(b)] at higher T_{ex} the line appears in emission; [(c)] using the IRAM 30m with no dilution; [(d)] using the NOEMA observations for Ellipse A; [(e)] using the NOEMA observations for Ellipse B.

55 km s^{-1}. The 2–1 and 3–2 transitions are both, to our knowledge, the first detections of the DCO^+ species seen in absorption. We were able to fit both narrow absorption lines to obtain constraints on the kinetic temperature and p-H_2 density using the collision rates provided by the BASECOL database[4], computed down to 5 K. For the absorption component, the density must be $\leq 10^5$ cm^{-3} (so that the 2–1 transition stays in absorption) and the kinetic temperature must be $\leq$10 K (or both transitions will appear in emission). In order to reproduce both transitions (2–1 and 3–2) with a fixed temperature of 10 K we need a density of 2.5×10^4 cm^{-3} (see Table 3). The ortho-para ratio of molecular hydrogen is a significant unknown; however, chemical studies for the cold and dense regions of the ISM have shown a low ortho-para ratio (Dislaire et al. 2012) compatible with deuterium enrichment (Pagani et al. 2009). The computed p-H_2 density is likely close to the H_2 density in the core study. From our DCO^+ observations, we can conclude that the absorption traces a dense cloud, which must be cold enough to become deuterated, along the line of sight. If DCO^+ had been detected with no background continuum, its line intensity for the 2–1 transition would have been 0.2 K. However, at such a large distance, such a small source would be heavily diluted in a single-dish telescope beam and would need observations with a mm interferometer. Absorption studies are best suited, and are not affected by beam dilution, as long as the absorbing layer is larger than the continuum.

For the $H^{13}CO^+$ transition we use the collision coefficients (down to 10 K) provided by the LAMDA database (Flower 1999). With only one transition, we fixed the temperature and density as estimated from DCO^+ to estimate the column density. Using a $^{12}C/^{13}C$ ratio of 68 (Milam et al. 2005), the resulting DCO^+/HCO^+ ratio is about 0.02.

DNC has also been detected in absorption against the CH_3OCHO transition (19(3, 17)–18(2, 16)) at 228.894 GHz emitted from the HII region. We used the collision coefficients from Dumouchel et al. (2011) available in the BASECOL database, and fixed the kinetic temperature at 10 K and the p-H_2 density at 2.5×10^4 cm^{-3}. We used the same strategy for $HN^{13}C$ which has been detected in absorption at the same velocity. The $DNC/HN^{13}C$ ratio is surprisingly high, ~9.2, resulting in a DNC/HCN ratio of 0.14 using the same assumptions as for DCO^+. However, Roueff et al. (2015) showed that the $^{12}C/^{13}C$ ratio in nitriles may be different from the isotopic ratio. Hence, the DNC/HNC ratio may be somewhat lower.

[4] http://basecol.obspm.fr/

The o-NH_2D species is the only deuterated species that we detected in emission at ~69 km s^{-1}. However, its velocity is slightly different from that of the other species, which makes it difficult to explain in terms of the geometry of the source. Assuming no beam dilution in our IRAM 30m beam we derived the column density within the [5−10] K range (see Table 3). However, our NOEMA observations of the same ortho-NH_2D transition, resulted in the detection of two adjacent cores. Using the same temperature range we also derive the column densities for both Ellipse A and Ellipse B detections (see Table 2).

The excitation of the two p-H_2CO transitions detected in absorption at about 69 km s^{-1} with our IRAM 30m observations is compatible with the physical conditions derived from DCO^+. The collisional rates used for p-H_2CO are taken from Wiesenfeld & Faure (2013), computed for temperatures as low as 10 K. The physical conditions derived from the detected transitions are slightly different from the values derived for CN by Mookerjea et al. (2014) with $T_K \sim 6$ K and $n(H_2) \sim 10^5$ cm^{-3}. However, owing to the physical complexity of the W51 molecular cloud complex, it is possible that we detected many components with different molecular probes (D-species versus CN). Also, with the contamination by the W51 molecular cloud complex, the CN line profiles were difficult to analyze, leading to a 50% uncertainty on the kinetic temperature and H_2 density.

3.2. Comparison with a typical dark cloud: TMC-1

The resulting temperature (10 K) and H_2 density (2.5×10^4 cm^{-3}) for the ~69 km s^{-1} narrow component is compatible with dark cloud conditions. Strong deuteration of molecules and ions (e.g., DNC and DCO^+) has been recognized as a landmark of these regions that are the birthplaces of low-mass stars. The molecule H_2 (respectively HD) is the main reservoir of hydrogen (respectively deuterium) in dark clouds. Gas-phase deuteration at low temperature is driven by the molecular ions H_2D^+ and D_2H^+ (Millar et al. 1989; Vastel et al. 2004), which play a major role in ≤20 K gas. In prestellar cores, the freezing of CO on grains implies a reduction of the production rate of HCO^+ since the main production route is the protonation of CO. However, for DCO^+, the significant increase in the abundance of H_2D^+, D_2H^+, and D_3^+ counterbalances the decrease in CO abundance. The DCO^+ abundance remains more or less constant, as shown by Vastel et al. (2006) in the case of L1544 and further discussed by Pagani et al. (2011). In the external layers of prestellar cores (radius between 5000 and 10 000 AU), where the density approaches 10^4 cm^{-3} and the kinetic temperature remains close to 10 K, the depletion of CO is less extreme than in the central region. These dark cloud conditions are well suited for the production of DCO^+.

We can now compare W51-core with TMC-1, a prototypical dark cloud located in the Taurus molecular cloud at a distance of 140 pc (Elias 1978; Onishi et al. 2002). The most massive molecular cloud in Taurus is the Heiles Cloud 2 (HCL 2; Heiles 1968; Onishi et al. 1996; Tóth et al. 2004). It hosts several cold clumps first recognized in extinction maps and recently detected by the Planck Collaboration XXVIII (2016). TMC-1 is a long and dark filament, running approximately SE to NW with a temperature of about 10 K and a mean column density of $\sim 2 \times 10^{22}$ cm^{-2} (Fehér et al. 2016). TMC-1 shows a remarkable variation in the chemical abundances; there are carbon chains and cyanopolyynes in the SE part, notably in the cyanopolyyne peak TMC(CP), and ammonia peaks in the NW regain, which shows a more evolved chemistry. Deuteration is lower in the CP region (Turner 2001) than in the ammonia peak (Tiné et al. 2000)

where $DCO^+/(H^{13}CO^+ \times 68) \sim 0.011$, which is similar to the value found for W51-core. However, the DNC/HNC ratio found by Hirota et al. (2001) is a factor of 5 lower than the value we found in W51-core (0.028 vs. 0.15).

3.3. Increased deuterium fractionation for HNC

Hirota et al. (2001) observed 29 nearby dark cloud cores and measured a large variation in the $DNC/HN^{13}C$ ratio between 0.5 and 7.3 (DNC/HNC = [0.01–0.11]). The lowest ratios correspond to the carbon-chain producing regions where CCS and cyanopolyynes are abundant. In addition, they found a gradient in TMC-1 where the $DNC/HN^{13}C$ ratio in the northwest part of the TMC-1 ridge including the NH_3 peak is found to be higher than that in the southeast part around the cyanopolyyne peak. These authors found no apparent relation between the $DNC/HN^{13}C$ ratio and the H_2 density and kinetic temperature, but concluded that the deuterium fractionation of DNC may be related to the chemical evolution of dark cloud cores.

These values are higher than those predicted by pure gas-phase chemical models for cold dark cloud cores (Roueff et al. 2015). The effect of the depletion of molecules onto grain surfaces is also invoked to explain the observed ratio. In the L1544 prestellar core, a large CO depletion was reported by Caselli (2002), leading to a high deuterium fractionation. The DCO^+/HCO^+ ratio is much enhanced toward the center of the core although the DNC/HNC ratio is constant throughout the cloud (Hirota et al. 2003), leading to the conclusion that DNC/HNC is not very sensitive to the depletion factor unlike DCO^+/HCO^+ and N_2D^+/N_2H^+. The variation in the $DNC/HN^{13}C$ ratios from core to core is much larger than that within each core. This variation might be related to the timescale of the deuterium fractionation and the observed variation from one core to another might be the combination of the three competing, time-dependent processes: gas-phase deuterium fractionation, depletion of molecules onto grain surfaces, and dynamical evolution of a core (see, e.g., Aikawa et al. 2001). The DNC/HNC ratio becomes higher for more chemically evolved cores.

More recently Sakai et al. (2012) has observed 18 massive clumps including infrared dark clouds (IRDCs) and high-mass protostellar objects (HMPOs). The averaged DNC/HNC ratio in HMPOs is lower than in IRDCs, with higher kinetic temperature for HMPOs. However, some of the IRDCs with a *Spitzer* 24 μm source show a lower DNC/HNC ratio than that of HMPOs, although the temperature is lower. This suggests that DNC/HNC does not depend on the kinetic temperature only. However, chemical models suggest that the DNC/HNC ratio decreases after the birth of protostars, depending on the physical conditions and history in their starless phase. More recent ALMA observations of IRDC G34.43+00.24 show a DNC/HNC of 0.06, which is significantly larger than the value of 0.003 determined from single-dish observations (Sakai et al. 2015). They suggest that single-dish observations may trace low-density envelopes while ALMA traces higher density and highly deuterated regions. Chemical model calculations from (Sakai et al. 2015), based on the chemical reaction network of Furuya et al. (in prep.), show that at a given time, the DNC/HNC abundance ratio is significantly higher in the dense core than in its immediate environment.

Additionally, Roueff et al. (2015) have shown that a higher ortho-para ratio for H_2 (typically in less dense regions) leads to a higher DNC/HNC ratio, demonstrating the complexity of the interplay between the chemistries of the species D, ^{13}C, and ^{15}N.

3.4. Distance of the W51-core

Infrared dark clouds have filamentary structures that are seen in absorption in the mid-infrared against the bright Galactic background. They are complexes of cold ($\leq$25 K) and dense ($\geq 10^{3-4}$ cm^{-3}) molecular gas within which cold cores of typical size 0.1 pc have recently been detected (e.g., Ragan et al. 2015). We possibly detected an IRDC as the filamentary structure in front of W51 where prestellar cores and their surrounding clump material are interacting. The absorption feature at 68 km s^{-1} has a velocity forbidden by the circular galactic rotation model (Schmidt 1965) and is thought to be due to the gas streaming along the spiral arm in the density-wave theory of galactic rotation.

According to the density-wave theory, the HV streaming gas is located near the subcentral point, but extends over 1.5 kpc along the line of sight (Koo 1997). All existing observations indicate that the HV stream is in front of the HII regions. Given that the stream shows evidence of interaction with the W51 main cloud triggering star formation it has to be physically interacting with the main cloud (Kang et al. 2010).

Thus, W51-core which we detect in the HV stream is likely located at a distance of not less than 4 kpc. This makes it the most distant dark cloud detected so far in the Galaxy. We can use $H^{13}CO^+$ as a probe of the total H_2 column density, with an HCO^+ abundance of 3×10^{-9} and a $^{12}C/^{13}C$ ratio of 68, leading to a value of $N(H_2) = 9 \times 10^{21}$ cm^{-2}, compatible with dark cloud conditions. From our NOEMA observations, two nearby fragments (separated by less than 10″, corresponding to about 0.19–0.24 pc at a distance of 4–5 kpc) have been identified. The fragments are compact, less than 0.16–0.19 pc in size (at a distance of 4–5 kpc). Recently, many high spatial resolution studies of IRDCs have led to the conclusion that these sources are highly fragmented, with regularly spaced cores; for example, the mean separation between the cores is 0.18 pc in IRDC G035.39–00.33 (Henshaw et al. 2016), 0.18 pc in G011.11–0.12 (Ragan et al. 2015), and (0.40 ± 0.18) pc in IRDC 18223 (Beuther et al. 2015). These values are compatible with our findings. We note that a detailed study of the fragmentation of the filament leading to the formation of the W51-core is limited because of the continuum and line contamination from the W51 compact HII region.

4. Conclusions

Combined *Herschel*/HIFI and IRAM 30m observations led to the detection of a distant dark cloud (4–5 kpc) along the line of sight of a compact HII region W51. This cloud, named W51-core, presents a fragmented structure that was determined from our IRAM/NOEMA observations of the NH_2D transition seen in emission and has two cores (less than 0.16–0.19 pc in size) separated by 0.19–0.24 pc. These high spatial observations of W51-core are consistent with a filamentary structure in front of W51, fragmenting while interacting with the giant molecular cloud, leading to the formation of many cold cores trailing along the filament. Our IRAM 30m observations led to the detection of W51-core in absorption against the strong continuum emitted by W51. Although not affected by beam dilution, absorption studies cannot trace the spatial extent of the source. From the IRAM 30m observations we derived the physical properties of W51-core with a density of $\sim 2.5 \times 10^4$ cm^{-3} and a temperature of about 10 K. It presents a high deuterium fractionation of HCO^+ (0.02) and HNC (0.14) with the first detection of DCO^+ in absorption. Because of its fortuitous location along the line

of sight with the continuum-bright W51e2 compact HII region, W51-core has not been detected in the continuum images. However, it makes it an appropriate source for absorption studies such as the search of H_2D^+, D_2H^+, and D_3^+.

Acknowledgements. C.V. is grateful for the help of the IRAM staff at Granada during the data acquisitions, and also for their dedication to the telescope. B.M. acknowledges the support received from University of Toulouse for her stay in Toulouse, which enabled the completion of this work. This work was supported by the CNRS program "Physique et Chimie du Milieu Interstellaire" (PCMI).

References

Aikawa, Y., Ohashi, N., Inutsuka, S., et al. 2001, ApJ, 552, 639
André, P., Men'shchikov, A., Bontemps, S., et al. 2010, A&A, 518, L102
Arnal, E. M., & Goss, W. M. 1985, A&A, 145, 369
Beuther, H., Ragan, S. E., Johnston, K., et al. 2015, A&A, 584, A67
Bieging, J. 1975, in H II Regions and Related Topics, eds. T. L. Wilson, & D. Downes (Berlin: Springer), Lect. Notes Phys., 42, 443
Caselli, P. 2002, Planet. Space Sci., 50, 1133
Carpenter, J. M., & Sanders, D. B. 1998, AJ, 116, 1856
Coutens, A., Vastel., C., Caux, E., et al. 2012, A&A, 539, A132
Coutens, A., Vastel., C., Cazaux, S., et al. 2013, A&A, 553, A75
Dislaire, V., Hily-Blant, P., Faure, A., et al. 2012, A&A, 537, A20
Dumouchel, F., Klos, J., & Lique, F. 2011, Phys. Chem. Chem. Phys., 13, 8204
Elias, J. H. 1978, ApJ, 224, 857
Fehér, O., Tóth, L. V., Ward-Thompson, D., et al. 2016, A&A, 590, A75
Flower, D. R. 1999, MNRAS, 305, 651
Habe, A., & Ohta, K. 1992, PASJ, 44, 203
Henshaw, J. D., Caselli, P., Fontani, F., et al. 2016, MNRAS, 463, 146
Heiles, C. E. 1968, ApJ, 151, 919
Hirota, T., Ikeda, M., & Yamamoto, S. 2001, ApJ, 547, 814
Hirota, T., Ikeda, M., & Yamamoto, S. 2003, ApJ, 594, 859
Kang, M., Bieging, J. H. Kulesa, C. A., et al. 2010, ApJS, 190, 58
Koo, B.-C. 1997, ApJS, 108, 489
Millar, T. J., Bennett, A., & Herbst, E. 1989, ApJ, 340, 906
Milam, S. N., Savage, C., Brewster, M. A., et al. 2005, ApJ, 634, 1126
Molinari, S., Swinyard, B., Bally, J., et al. 2010, A&A, 518, L100
Mookerjea, B., Vastel, C., Hassel, G., et al. 2014, A&A, 566, A61
Neill, J. L., Wang, S., Bergin, E. A., et al. 2013, ApJ, 770, 142
Onishi, T., Mizuno, A., & Kawamura, A. 1996, ApJ, 465, 815
Onishi, T., Mizuno, A., Kawamura, A., et al. 2002, ApJ, 575, 950
Pagani, L., Vastel, C., Hugo, E., et al. 2009, A&A, 494, 623
Pagani, L., Roueff, E., & Lesaffre, P. 2011, ApJ, 739, L35
Planck Collaboration XXVIII. 2016, A&A, 594, A28
Ragan, S. E., Henning, T., Beuther, H., et al. 2015, A&A, 573, A119
Roueff, E., Loison, J.-C., & Hickson, K. 2015, A&A, 576, A99
Sakai, T., Sakai, N., Furuya, K., et al. 2012, ApJ, 747, 140
Sakai, T., Sakai, N., Furuya, K., et al. 2015, ApJ, 803, 70
Sato, M., Reid, M. J., Brunthaler, A., & Menten, K. M. 2010, ApJ, 720, 1055
Sollins, P. K., Zhang, Q., & Ho, P. T. P. 2004, ApJ, 606, 943
Schmidt, M. 1965, Galactic structure, eds. A. Blaauw, & M. Schmidt (Chicago: Univ. Chicago Press)
Tiné, S., Roueff, E., Falgarone, E., et al. 2000, A&A, 356, 1039
Tóth, L. V., Haas, M., Lemke, D., et al. 2004, A&A, 420, 533
Turner, B. E. 2001, ApJ, 136, 579
Vastel, C., Phillips, T. G., & Yoshida, H. 2004, ApJ, 606, L127
Vastel, C., Caselli, P., Ceccarelli, C., et al. 2006, ApJ, 645, 1198
Vastel, C., Bottinelli, S., Caux, E., Glorian, J.-M., & Boiziot, M. 2015, SF2A-2015: Proceedings of the Annual meeting of the French Society of Astronomy and Astrophysics, eds. F. Martins, S. Boissier, U. Buat, L. Cambrésy, & P. Petit, 313
Wiesenfeld, L., & Faure, A. 2013, MNRAS, 432, 2573